Wiley Online Library
Early View publication on www.wileyonlinelibrary.com
(issue and page numbers not yet assigned;
citable using Digital Object Identifier – DOI)

J. Biophotonics 1–7 (2016) / **DOI** 10.1002/jbio.201500267

Journal of BIOPHOTONICS

FULL ARTICLE

Kinetic analysis of nanoparticle-protein interactions using a plasmon waveguide resonance

Farshid Bahrami[*,1], *Mathieu Maisonneuve*[2], *Michel Meunier*[2], *Arthur O. Montazeri*[1], *Yujin Kim*[1], *Nazir P. Kherani*[1], *J. Stewart Aitchison*[1], *and Mo Mojahedi*[1]

[1] Department of Electrical and Computer Engineering, University of Toronto, Ontario, M5S 3G4, Canada
[2] Department of Engineering Physics, Ecole Polytechnique de Montreal, Montreal, H3C 3A7, Canada

Received 4 October 2015, revised 19 December 2015, accepted 11 January 2016
Published online 15 February 2016

Key words: Plasmon waveguide resonance, Protein-nanoparticle interactions, SPR sensor, Biosensing

A plasmon waveguide resonance (PWR) sensor is proposed for studying the interaction between gold nanoparticles and proteins. The ability of the PWR sensor to operate in both TM and TE Polarizations, i.e. its polarization diversity, facilitates the simultaneous spectroscopy of the nanoparticles surface reactions using both polarizations. The response of each polarization to streptavidin-biotin binding at the surface of gold nanoparticles is investigated in real time. Finally, using the principles of multimode spectroscopy, the nanoparticle's surface reactions are decoupled from the bulk solution refractive index variations.

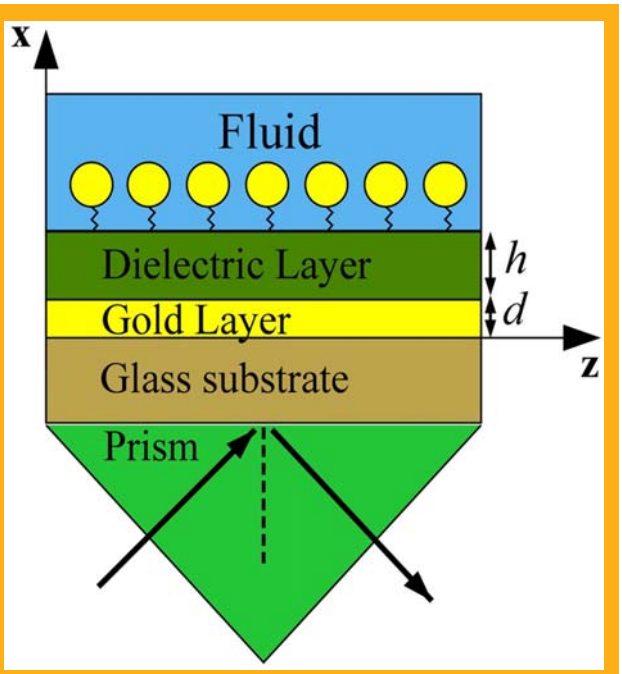

Schematic diagram of the NP-modified PWR sensor

1. Introduction

Nanoparticles (NPs) have attracted much interest due to their unique chemical and physical properties [1]. They are finding applications in many areas including electronics, medicine, textiles, cosmetic products, and so on [2]. The development of NPs as drug carriers and imaging agents in the biomedical

* Corresponding author: e-mail: farshid.bahrami@mail.utoronto.ca

field makes them a novel functional material [3, 4]. Their small size enables them to pass through biological membranes and interact with biomolecules such as proteins. The interaction between NPs and proteins can alter the protein conformation, thus affecting the cellular functionality, resulting in toxicity [5]. Consequently, there is a growing concern about NP toxicity and biocompatibility which compels further investigation of protein-NP interaction [6, 7].

The interactions between NPs and proteins are dynamic events marked with continuous association and disassociation processes, where the rates of these processes depend on the protein and particle types. Several methods have been used to investigate the NP-protein interactions, including measurements of binding affinity and ratios [8, 9], conformational variations [10, 11], and kinetic binding properties of the NP-protein interactions [5, 12]. Surface plasmon resonance (SPR) is one of the most well-known and commonly used techniques to study NP-protein binding kinetics [5]. However, the SPR technique has some drawbacks. The underlying gold film which is in direct contact with NPs has a large thermal conductivity [13] which can create thermal fluctuations [14, 15]. This effect can cause thermal denaturing [16] of the protein layer resulting in false measurement results. Moreover, resonance broadening of the NP-modified SPR sensor [17], caused by the increase in surface plasmon damping [18], also undermines the accuracy of detecting the resonance angle. This problem is less significant in quartz crystal microbalance method which is another technique for real-time kinetic analysis [12, 19].

In this paper, we propose a new approach for kinetic study of the NPs based on a plasmon waveguide resonance (PWR) sensor. A PWR sensor consists of a thin metallic layer loaded with a thick dielectric layer that can simultaneously guide both TM and TE polarized modes [15]. The ability to carry out spectroscopic measurements using two orthogonal polarizations with sharp resonances, instead of one broad resonance in the case of SPR sensor (only TM polarization), allows the PWR sensor to extract more information with better accuracy from the specimen. Furthermore, the presence of the thick dielectric layer between the metal film and the specimen reduces the aforementioned thermal heat effects of the metal on the analyte [15]. Finally, to study the AuNP-protein interactions, the AuNPs can be functionalized while immobilized on the sensing layer (top dielectric) of the PWR sensor. On the other hand, in the case of SPR, both the sensing surface and NPs' material are gold which requires functionalization of the AuNPs prior to the immobilization on the sensing layer in order to only allow for interaction between NPs (but not the sensing surface) and the target molecules. As a proof of concept, interactions between biotinylated-AuNPs of two different sizes with streptavidin protein are investigated via dual polarization spectroscopy.

2. Principle of operation

Figure 1(a) shows the schematic of the PWR sensor based on Kretschmann configuration in which the AuNPs are immobilized on the top surface. The light is incident on the substrate through a prism and the reflected light intensity is measured as a function of the incident angle. Two different resonance modes (TM and TE) can be excited based on the polarization of the incident light. The field profiles of both TM and TE modes are shown in Figure 1(b). As the figure shows, the TM mode has a larger penetration depth into the fluid (up to 9 μm) while the TE mode is mostly confined within the dielectric layer with a small tail (up to 300 nm) extending into the fluid. The sharp resonances of the PWR modes [Figure 1(c)] can be used to improve the accuracy of the sensor by reducing the standard deviation of the output signal [15].

Any refractive index variation on the surface of NPs or inside the bulk fluid alters the propagation

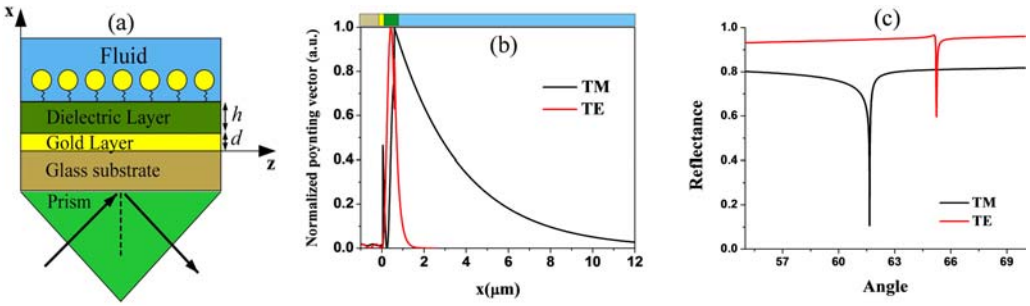

Figure 1 (**a**) Schematic diagram of the NP-modified PWR sensor. (**b**) z-component of the Poynting vector for both TM and TE polarizations in the optimized PWR sensor at the resonance angles of 61.65° and 65.23°, respectively. (**c**) Reflectance spectrum for the optimized PWR-TM and PWR-TE in black and red lines, respectively. The fluid refractive index is 1.33.

constant of the modes by different amounts due to the difference in their field profiles. This difference in response of each mode to the surface or bulk properties manifest as a change in the resonance angle ($\Delta\theta_{TM}$ or $\Delta\theta_{TE}$) and can be used to decouple the surface and bulk effects. Assuming that the resonance angle shifts are linearly dependent on the surface and bulk effects and that the sensitivity factors are known (calculated from simulation or measured during calibration process), variations in the protein concentration surrounding the NP surface (Δc) and the bulk refractive index change (Δn_B) can be differentiated using the following equations [20]:

$$\Delta n_B = \frac{SF_{TM}^{bulk} \times \Delta\theta_{TE} - SF_{TE}^{bulk} \times \Delta\theta_{TM}}{SF_{TM}^{bulk} \times SF_{TE}^{surf} - SF_{TM}^{surf} \times SF_{TE}^{bulk}} \quad (1)$$

$$\Delta c = \frac{SF_{TE}^{surf} \times \Delta\theta_{TM} - SF_{TM}^{surf} \times \Delta\theta_{TE}}{SF_{TM}^{bulk} \times SF_{TE}^{surf} - SF_{TM}^{surf} \times SF_{TE}^{bulk}} \quad (2)$$

Where, SF_{TM}^{bulk} and SF_{TE}^{bulk} are the bulk sensitivity factors in degree/refractive index unit (RIU) for the TM and TE polarizations, respectively; and SF_{TM}^{bulk} and SF_{TE}^{bulk} are the surface sensitivity factors in degree/concentration for the TM and TE polarizations, respectively [21].

Theoretically, the bulk sensitivity factor can be determined by calculating the change in resonance angle due to the change in bulk fluid refractive index. On the other hand, the surface sensitivity factor can be estimated by calculating the change in resonance angle due to the change of refractive index in the NPs' surrounding medium within a few nanometers from the dielectric-fluid interface (while the bulk solution refractive index remains unchanged). In order to calculate the surface and bulk sensitivity factors, a transfer matrix method is used to determine the reflectance from a multilayer structure along with an effective medium theory to model the nanoparticle arrays embedded in a homogenous medium. The effective medium model used here is based on the Maxwell-Garnett effective medium theory [22], which is useful in estimating the effective permittivity of random composites. Accordingly, the effective index of AuNP arrays embedded in a solution of water can be expressed as:

$$\varepsilon_{eff} = \varepsilon_f \frac{\varepsilon_g(1+2f) + 2\varepsilon_f(1-f)}{\varepsilon_g(1-f) + \varepsilon_f(2+f)} \quad (3)$$

where, f is the filling fraction of the AuNPs (ε_g) inside the fluid (ε_f). The theoretical and experimental results are discussed in Section 4.

3. Experimental setup

3.1 Sensors fabrication and functionalization

We obtained 1 cm × 1 cm BK7 glass substrates coated with 48 ± 1 nm gold layer [Figure 2(a)] from the SSENS Ltd. [23]. These samples were initially cleaned with a piranha solution at 90 °C for 20 min to remove organic contaminations. After the initial cleaning, the samples were further cleaned in an ultrasonic bath with acetone, isopropanol, and deionized (DI) water for 10 minutes each. To fabricate the PWR sensors, a silica layer of 550 ± 5 nm thickness which is close to the optimized thickness of 545 nm [5] was deposited on the gold film using a plasma enhanced chemical vapor deposition (PECVD) by mixing silane (SiH_4) and nitrous oxide (N_2O) in vacuum at approximately 300 °C [Figure 2(b)]. The PWR sensors were then rinsed with DI water and ethanol and incubated at room temperature in a solution of a bifunctional siloxane 3-aminopropyltrimethoxysilane (APTMS; 1 mMin ethanol) for 10 minutes and then spun out at 2000 rpm for 30 sec to uniformly cover the sensor with a layer of APTMS [Figure 2(c)]. The sensors were then rinsed

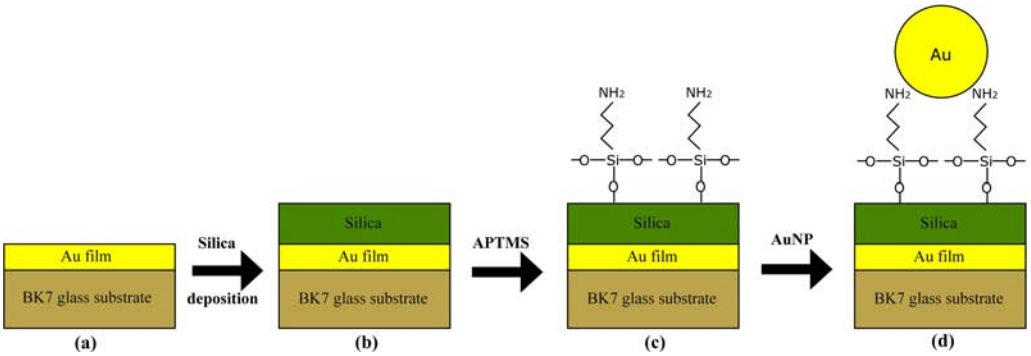

Figure 2 (**a**) Schematic diagram of the BK7 glass substrate with 48 nm of gold film. (**b**) Deposition of 550 nm silica on the gold film using PECVD. (**c**) The PWR sensor coated with a layer of APTMS. (**d**) Binding AuNPs on the APTMS.

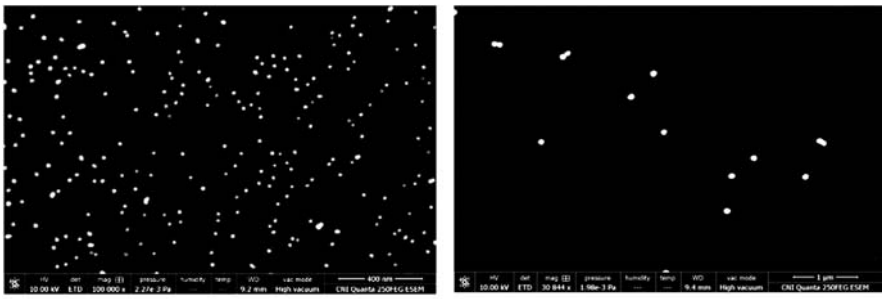

Figure 3 SEM images of the gold nanoparticles on the PWR sensor with diameters of (**a**) 20 nm with surface density of 7.6×10^9 particles/cm^2, and (**b**) 100 nm with surface density of 3.7×10^7 particles/cm^2.

with ethanol, DI water, N_2 dried, and placed in a 100 °C oven for 1 hour to complete Si–O bond formation. The AuNPs were assembled on the sensor surface by incubating the sensors with AuNP solution for 10 minutes [Figure 2(d)]. The samples were then spun out at 2000 rpm for 30 sec, rinsed with DI water, N_2 dried, and placed in a 100 °C oven for 1 hour to improve the affinity between the AuNPs and APTMS.

Two different solutions of AuNPs with two different sizes (20 nm and 100 nm) were immersed on the PWR sensors. Figure 3(a) and (b) shows the SEM images of the AuNPs immobilized on the PWR sensors with diameters of 20 nm and 100 nm and surface densities of 7.6×10^9, and 3.7×10^7 particles/cm^2, respectively.

3.2 Instrumentation

Figure 4(a) shows the optical setup used to characterize performance of the PWR sensor. A super continuum laser beam (Fianium SC-450) is passed through a tunable filter (Photon Etc) and a single mode optical fiber. The light is then directed through an achromatic lens (L1) in order to collimate the light rays. The collimated light is then passed through a system composed of a linear polarizer and a liquid crystal variable retarder acting as a polarization switch. A second achromatic lens (L2) is used in order to achieve a converging beam to cover a desired range of angles. The converging beam is focused on the PWR sensor which is attached with immersion oil (Cargile Lab) to the back surface of the prism. The diverging light that is reflected from the sample (sensor) surface is collected by a CMOS camera (Thorlabs Inc.) to analyze the angular spectrum of the beam intensity. A Labview program was written to process images recorded by the CMOS camera, which in addition determined the minimum position of the angular curves by using a polynomial interpolation.

Figure 4(b) shows the normalized reflectance spectrum (R_{TM}/R_{TE}) obtained from the PWR sensors covered with 20 nm and 100 nm AuNPs at the optimized wavelengths of 780 nm and 720 nm, respectively. The optimized wavelengths and layers' thicknesses are obtained with an in-house code using a genetic algorithm. The first resonance for both samples appears close to 61° and corresponds to the TM mode. The second resonance appears close to 67° which corresponds to the TE mode, but since the TE reflectance is in the denominator it appears as a peak in the normalized spectrum.

4. Results and discussion

In order to use the PWP sensor to investigate the NP-protein interactions we have used the biotin-streptavidin complex, as it provides a strong affinity and high specificity of interaction. To functionalize the AuNPs with biotin, a solution of biotinylated PEG alkane thiol is passed over the PWR surface (covered with AuNPs) for two hours. The functionalized sensor is then fixed between the prism and

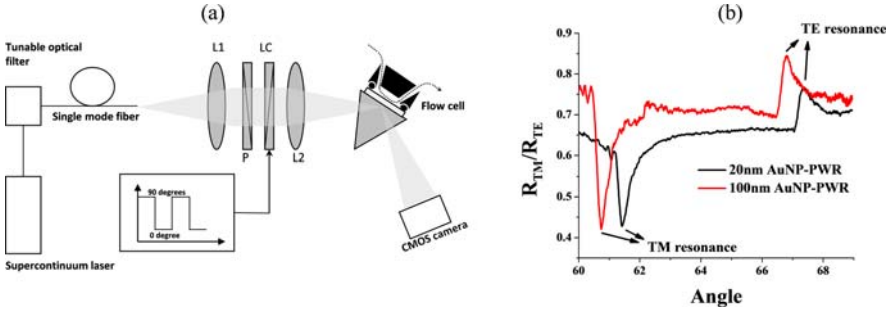

Figure 4 (**a**) Optical setup used to detect the resonance angles. (**b**) The normalized reflectance spectrum measured for 20 nm and 100 nm AuNPs immobilized on the PWR sensor.

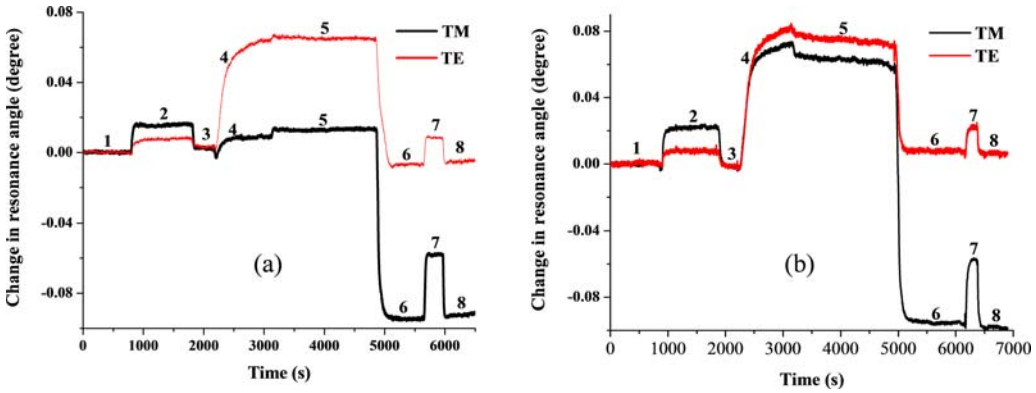

Figure 5 Angular positions of the resonance angles vs. time for (**a**) 20 nm and (**b**) 100 nm AuNP immobilized on the PWR sensor. Solutions are (1) PBS, (2) 1 μg/mL Streptavidin, (3) PBS, (4) 10 μg/mL Streptavidin, (5) PBS, (6) DI water, (7) 1% ethanol, and (8) DI water.

the flow cell [Figure 4(a)] using the oil matching index.

The FWHM of the resonance modes in the PWR sensor with AuNPs on top is 0.45 degree for TM polarization and 0.44 degree for TE polarization. This is larger than the FWHM of the PWR sensor without AuNP (0.32 degree for TM polarization and 0.31 degree for TE) due to the increased surface roughness in the presence of nanoparticles which increases the radiation loss and therefore widens the resonance bandwidth [20].

Figure 5 shows the measured sensograms which are the result of attaching streptavidin to the biotinylated AuNPs of two different sizes. Each sensogram is obtained at different wavelength – since the optimized wavelength, that provides the narrowest resonance for each mode, is different for different sizes of AuNPs. These wavelengths are 780 nm for the 20 nm AuNP-PWR and 720 nm for the 100 nm AuNP-PWR.

In all experiments, phosphate buffered saline (PBS) solution is used as the buffer for the streptavidin diluted solution. The solutions are introduced to the sensor in the following order: (1) First a pure PBS solution is passed over the sample for 25 minutes to create a baseline. (2) A streptavidin solution with concentration equal to 1 μg/ml is passed during 25 minutes in the flow cell to study the sensor response to a low concentration of the analyte. (3) A rinsing step is introduced for 10 minutes by flowing pure PBS solution to dissociate the weakly bounded molecules from the surface. (4) 10 μg/ml streptavidin solution is passed for another 25 minutes to get a streptavidin saturated surface. (5) Another rinsing step is performed. (6) At this point, to investigate the response of PWR sensor to variations in the bulk refractive index only, the PBS buffer solution is switched to the deionized water (DI, MilliQ 18.2 MΩ cm). (7) 1% Vol. ethanol solution (water diluted) is passed for 5 minutes. (8) Finally, DI water flows over the sample to recreate the baseline.

As evident from the Figure 5(a), the TM mode is more sensitive to the bulk index variations which can be seen by comparing the changes in resonance angles when the PBS buffer solution is switched to the DI water (step 5 to 6 in Figure 5), or equally well, when the DI water is switched to 1% ethanol solution and back to the DI water (steps 6 to 7 and 7 to 8 in Figure 5). Stronger sensitivities of the TM mode to the bulk and the TE mode to the surface variations are in agreement with the theoretical results depicted in Figure 1(b), where the TM mode penetrates longer distances into the solution whereas the TE mode is more tightly bounded to the surface.

Table 1 displays theoretically calculated and ?experimentally measured ratios of the surface and bulk sensitivities for two different AuNP sizes (20 and 100 nm). While the agreement between theory and experiment is good, results for the 20 nm AuNP

Table 1 Comparison between experimental and theoretical values of the sensitivities' ratio.

Method	20 nm AuNP-PWR		100 nm AuNP-PWR	
	$\frac{SF_{TE}^{surf}}{SF_{TM}^{surf}}$	$\frac{SF_{TE}^{bulk}}{SF_{TM}^{bulk}}$	$\frac{SF_{TE}^{surf}}{SF_{TM}^{surf}}$	$\frac{SF_{TE}^{bulk}}{SF_{TM}^{bulk}}$
Experiment	5.33	0.4	1.17	0.38
Theory	5.6	0.32	1.05	0.36

Table 2 Variations in wavevectors due to perturbation of the refractive index of AuNPs, surrounding medium.

Polarization	δk: 20 nm AuNP	δk: 100 nm AuNP
TE mode	3.9×10^4	2×10^5
TM mode	3.4×10^3	1.5×10^5

shows that, when sensing surface properties, the TE mode is 5.33 times more sensitive than the TM <? A3B2 twb.mode. On the other hand, the TM mode is 2.5 = 1/0.4 times more sensitive than the TE mode when sensing bulk index variations. However, in the case of 100 nm AuNP both TE and TM modes have similar surface sensitivities, although not the same bulk sensitivities. The change in resonance angle and the change in the solution refractive index are determined with accuracy of 0.05 degree and 8.2×10^{-6} RIU, respectively.

The fact that surface sensitivity of the TE mode is 5.6 times larger than the TM mode for the 20 nm AuNPs, while in the case of 100 nm these surface sensitivities are almost equal (1.05), can be understood in terms of variations of the wavevector (δk). These variations for the TM and TE modes, which are proportional to the overlap integral [24], can be calculated from

$$\delta k \approx \frac{k_i}{2} \frac{\int_{V_{in}} \delta\varepsilon \cdot \boldsymbol{E}_i^* \cdot \boldsymbol{E}_f \cdot \mathrm{d}r}{\int_V \varepsilon \cdot \boldsymbol{E}_i^* \cdot \boldsymbol{E}_i \cdot \mathrm{d}r} \tag{4}$$

In Eq. (4), E_i and k_i are the electric field and its wavevector before the change in refractive index due to surface binding, E_f is the electric field after the change in refractive index, V_{in} is the volume of interaction between the field and the analyte, V is the total volume covered by the field, and δk is the change in wavevector due to the change in permittivity of the analyte (from ε to $\varepsilon + \delta\varepsilon$). Table 2 summarizes the changes in wavevectors for both modes of each sample which is calculated using Eq. (4) and by estimating the field profiles from a transfer matrix method in which Maxwell–Garnett theory is used to replace the AuNPs with an effective medium.

As data in Table 2 shows changes in the overlap integral between the TM and TE modes in the case of 20 nm AuNPs is much larger (91%) than the case for 100 nm AuNPs (25%). In other words, calculations of the overlap integral also indicate that the difference between the surface sensitivities of the TE and TM modes are larger in the case of smaller AuNPs. Lastly, the difference between the theoretical and experimental values in Table 1 is due to several factors such as AuNPs aggregation, their non-uniform surface coverage, the presence of APTMS layer which was not included in the simulation, and the fabrication imperfections.

As stated earlier polarization diversity is an important advantage of the PWR sensors which allows the user to decouple the bulk and surface effects. Figures 6(a) and (b) demonstrate this capability by applying the linear model of Eqs. (1) and (2) to the data displayed in Figure 5(a) and (b). The black lines in Figure 6(a) and (b) signify the changes in surface binding concentrations which increase with attachment of the streptavidin to biotinylated AuNPs (steps 1 to 5 in Figure 6), and remain relatively constant when only bulk refractive index is changed (steps 6 to 8 in Figure 6). On the other hand, the blue lines in Figure 6(a) and (b), signify the changes in bulk (buffer) refractive index which

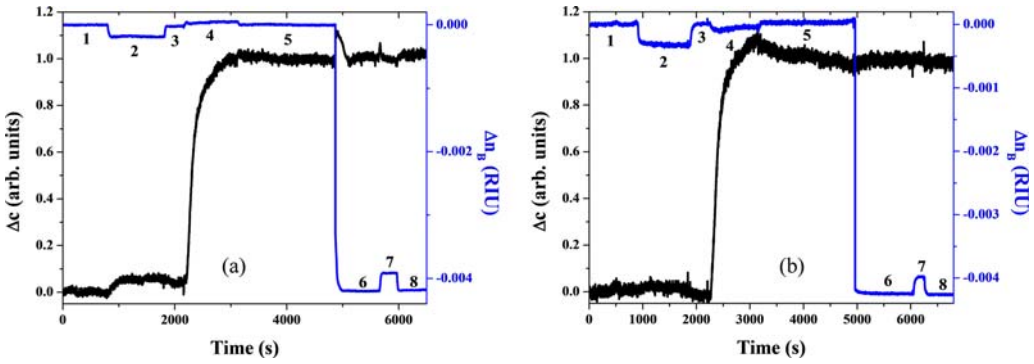

Figure 6 Decoupled surface binding concentrations (Δc) and bulk index variations (Δn_{B}) as a function of time for (a) 20 nm AuNP-PWR sensor and (b) 100 nm AuNP-PWR sensor. Solutions are (1) PBS, (2) 1 μg/mL Streptavidin, (3) PBS, (4) 10 μg/mL Streptavidin, (5) PBS, (6) DI water, (7) 1% ethanol, and (8) DI water.

mostly take place during the transition from step 5 to 6 and onward to step 8. In short, with the help of dual mode spectroscopy, made possible via PWR platform, the changes in protein concentration on the AuNPs can be decoupled from the variations in bulk refractive index.

5. Conclusion

A new approach for studying nanoparticle-protein interactions was proposed based on a PWR sensor. The AuNPs were immobilized on the PWR sensor and then functionalized with biotin. The polarization diversity of the PWR was utilized for dual-polarization spectroscopy of streptavidin interactions with biotinylated-AuNP. Two different AuNPs were immobilized on two different PWR sensors, one with diameter of 20 nm and surface density of 7.6×10^9 particles/cm^2 and the other with diameter of 100 nm and surface density of 3.7×10^7 particles/cm^2. Responses of the TE and TM modes to variations of the bulk refractive index and changes in the nanoparticle-protein binding concentration were monitored in real time for both samples. Finally, a linear model was used to decouple the AuNP surface binding concentration from bulk index variations.

Acknowledgements This work was supported by the Natural Science and Engineering Research Council of Canada–Biopsys Network under grant no. 486537 and also by CMC Microsystems (MNT financial assistant) under reference ID no. 1377.

References

[1] M. S. Khan, G. D. Vishakante, and H. Siddaramaiah, Adv. Colloid Interface Sci. **199–200**, 44–58 (2013).
[2] T. Tsuzuki, Int J Nanotechnol **6**, 567–578 (2009).
[3] S. Patskovsky, E. Bergeron, and M. Meunier, J. Biophotonics **8**(5), 401–407 (2013).
[4] G. L. Prasad, Safety of Nanoparticles, T. J. Webster, Ed., ed: Springer New York, 89–109 (2009).
[5] T. Cedervall, I. Lynch, S. Lindman, T. Berggård, E. Thulin, H. Nilsson, K. A. Dawson, and S. Linse, Proc Natl Acad Sci USA **104**, 2050–2055 (2007).
[6] A. Nel, T. Xia, L. Mädler, and N. Li, Science **311**, 622–627 (2006).
[7] I. Lynch and K. A. Dawson, Nano Today **3**, 40–47 (2008).
[8] X. Jiang, J. Jiang, Y. Jin, E. Wang, and S. Dong, Biomacromolecules **6**, 46–53 (2005).
[9] L. Shang, Y. Wang, J. Jiang, and S. Dong, Langmuir **23**, 2714–2721 (2007).
[10] X. C. Shen, X. Y. Liou, L. P. Ye, H. Liang, and Z. Y. Wang, J. Colloid Interface Sci **311**, 400–406 (2007).
[11] B. C. Braden, F. A. Goldbaum, B. X. Chen, A. N. Kirschner, S. R. Wilson, and B. F. Erlanger, Proc. Natl. Acad. Sci. USA **97**, 12193–12197 (2000).
[12] A. E. Gerdon, D. W. Wright, and D. E. Cliffel, Anal. Chem. **77**, 304–310 (2005).
[13] H. D. Young, R. A. Freedman, and L. Ford, Sears and Zemansky's University Physics, Addison-Wesley (2008).
[14] H. T. Huang, C. Y. Huang, T. R. Ger, and Z. H. Wei, Appl. Phys. Lett **102**, 111109 (2013).
[15] F. Bahrami, M. Maisonneuve, M. Meunier, J. Stewart Aitchison, and M. Mojahedi, Opt Express **21**, 20863–20872 (2013).
[16] J. H. Teichroeb, J. A. Forrest, and L. W. Jones, Eur. Phys. J. E Soft Matter **26**, 411–415 (2008).
[17] N. H. Kim, T. W. Kim, and K. M. Byun, Opt Express **22**, 4723–4730 (2014).
[18] S.-H. F.-C. Yi-Jun Jen and Fu-Ken Liu, Jpn. J. Appl. Phys. **45**, 1850–1852 (2006).
[19] L. Li, Q. Mu, B. Zhang, and B. Yan, Analyst **135**, 1519–1530 (2010).
[20] F. Bahrami, M. Z. Alam, J. S. Aitchison, and M. Mojahedi, Plasmonics **8**, 465–473 (2013).
[21] F. Bahrami, M. Maisonneuve, M. Meunier, J. S. Aitchison, and M. Mojahedi, Biomed. Opt. Express **5**, 2481–2487 (2014).
[22] Viktor Myroshnychenko, Jessica Rodríguez-Fernández, Isabel Pastoriza-Santos, Alison M. Funston, Carolina Novo, Paul Mulvaney, Luis M. Liz-Marzán, and F. Javier García de Abajo, Chem. Soc. Rev. **37**, 1792–1805 (2008).
[23] http://www.ssens.nl/.
[24] A. Shalabney and I. Abdulhalim, Sens. Actuators A **159**, 24–32 (2010).